ACS APPLIED ELECTRONIC MATERIALS

pubs.acs.org/acsaelm Article

Terahertz Antenna Impedance Matched to a Graphene Photodetector

François Joint,* Kunyi Zhang, Jayaprakash Poojali, Daniel Lewis, Michael Pedowitz, Brendan Jordan, Gyan Prakash, Ashraf Ali, Kevin Daniels, Rachael L. Myers-Ward, Thomas E. Murphy, and Howard D. Drew*

Cite This: *ACS Appl. Electron. Mater.* 2024, 6, 4819−4825 Read Online

ACCESS | Metrics & More | Article Recommendations | Supporting Information

ABSTRACT: Developing low-power, high-sensitivity photodetectors for the terahertz (THz) band that operate at room temperature is an important challenge in optoelectronics. In this study, we introduce a photothermal-electric effect detector based on quasi-free-standing bilayer graphene on a silicon carbide substrate, designed for the THz frequency range. Our detector's performance hinges on a quasi-optical coupling scheme, which integrates an aspherical silicon lens, to optimize impedance matching between the THz antenna and the graphene p−n junction. At room temperature, we achieved a noise equivalent power of less than 300 pW/$\sqrt{\mathrm{Hz}}$. Through an impedance matching analysis, we coupled a planar antenna with a graphene p−n junction, inserted in parallel to the nanogap of the antenna, via two coupling capacitors. By adjusting the capacitors and the antenna arm length, we tailored the antenna's maximum infrared power absorption to specific frequencies. The sensitivity, spectral properties, and scalability of our material make it an ideal candidate for future development of far-infrared detectors operating at room temperature.

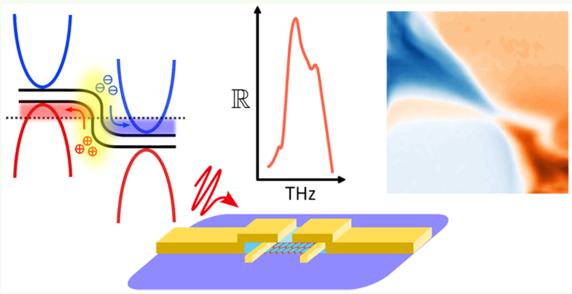

KEYWORDS: *Terahertz sensors, Graphene, Photothermo-electric effects, Planar Antenna, Far-infrared*

■ INTRODUCTION

Far-infrared detectors and heterodyne mixers that operate at room temperature are crucial for the deployment on resource-limited platforms such as observation satellites,[1] balloons, and small-satellites. These components are pivotal in advancing astrophysical and planetary heterodyne receivers. The main elements of optical receivers—the detector, the local oscillator (LO),[2] the first amplifier,[3] and the back-end electronics[4]—must all be state-of-the-art. Space missions, in particular, require components that are low in mass and volume and can operate within the constraints of limited cooling power (typically ≤100 mW at 4 K) and overall mission power. Therefore, sensors and instrumentation that dissipate low power and can operate at higher temperatures are desirable.

Graphene, known for its high room-temperature carrier mobility, substantial current flux, and high saturation velocity, emerges as an excellent candidate for low-power dissipation and consumption in terahertz (THz) electronics. Various detection mechanisms in graphene photodetectors for the THz frequency range have been explored, including the bolometric effect,[5−7] photo-thermoelectric effect,[8−11] Dyakonov-Shur (DS) rectification,[12−14] ballistic rectification,[15,16] and thermo-pile.[17] At cryogenic temperatures, the hot-electron effect in graphene is well-established, where strong electron−electron interactions lead to significant temperature dependence in graphene's conductivity σ, thereby affecting the resistance $R(T)$ and supporting the development of low-temperature bolometers.[6,7] Conversely, at room temperature, the hot-carrier-assisted photo-thermoelectric (PTE) effect is notably efficient due to effective carrier heating and significant electronic temperature gradients ($\Delta T_e \approx 1000$ K[6]), enhanced by the high Seebeck coefficient ($S \approx 100\ \mu$V/K[18−20]).

The efficacy of these detection systems heavily depends on the quasi-optical coupling efficiency between the incident THz field and the graphene detector. When integrated with planar antennas, the impedance mismatch between the antenna and the graphene sensing region could critically impair the performance of THz detection systems. Various antenna-integrated graphene-based photodetectors have been reported, utilizing configurations such as dipole,[9,10] broadband log-spiral,[10,11,13] and split-bowtie antennas.[21] These detectors use graphene grown via chemical vapor deposition (CVD) on a substrate of 300 nm SiO_2 over low-doped Si (100−250 Ω·cm),

Received: May 13, 2024
Revised: May 21, 2024
Accepted: May 21, 2024
Published: May 30, 2024

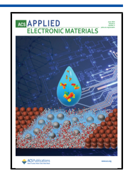

https://doi.org/10.1021/acsaelm.4c00870
ACS Appl. Electron. Mater. 2024, 6, 4819−4825

achieving external voltage responsivities ($\mathbb{R} = V_{ph}/P_{in}$) of up to $\approx$15 V/W at zero bias voltage with a split bow-tie antenna architecture. Enhancing $\mathbb{R}$ necessitates antennas with a large effective aperture area and correspondingly high gain, and a flat impedance over a wide range of frequencies is desirable. Therefore, optimizing the interface between the graphene detector and the antenna is crucial to minimize coupling losses, and particular attention must be paid to improving the impedance matching between these components. Conventional configurations connect the graphene sensor electrically to the two poles of the antenna,[6,9,12] but their performance rapidly deteriorates at very high frequencies due to impedance mismatch, while the detector's spectral properties remain narrow band.[12,22,23] Overcoming these challenges, such as by using high-mobility hBN encapsulated single-layer graphene (SLG) or bilayer graphene (BLG) and optimizing contact resistance, could reduce the limiting effects of thermal noise in graphene detectors.

According to the Wiedemann–Franz law and the Mott relation, the electron thermal conductivity (κ) of graphene can be expressed as $\kappa = L\sigma T$, where σ is the conductivity and L, the Lorentz number, is defined as $L = (\pi^2 k_B^2)/(3e^2)$. The Seebeck coefficient (S) is given by $S = LT(\partial \ln \sigma/\partial E_F)$, linking it directly to changes in conductivity with respect to the Fermi energy (E_F). When a thermal difference (ΔT_e) is induced, it results in a voltage $V = -S\Delta T_e$ and a heat flux to the substrate $Q = G_{th}A\Delta T_e$.

For conditions where $T \ll T_F = E_F/k_B$, the responsivity $\mathbb{R} = V/Q$ simplifies to approximately $\mathbb{R} = 2/(\sigma E_F)$. Hence, maximizing $\mathbb{R}$ for the photodetector requires minimizing both σ and E_F. With residual doping levels of epitaxial graphene on SiC near the Dirac point achieving $n_0 \leq 10^{10}$ cm^{-2},[7] this suggests a potential maximum responsivity of $\mathbb{R} \simeq 10^3$ V/W.

Increasing the T_e gradient through enhanced optical absorption can locally augment heat absorption in the BLG.[8] This enhancement was facilitated by integrating sub-wavelength nanogap confinement and boosting the near-field light–matter interaction, previously demonstrated to elevate responsivity.[9,24−26] Notably, $\mathbb{R}$ is inversely proportional to the thermal conductance (G_{th}); thus, a low G_{th} is critical for high sensitivity in THz detection. While epitaxial single-layer graphene (SLG) has shown $G_{th} \simeq 10^4$ W/K·m^2 at 6K,[27] significantly lower than SLG on SiO_2,[28] our quasi-free-standing BLG could potentially exhibit similar or even lower G_{th}.

Using a simplified model of PTE detector operation with uniform carrier density across the p–n junction, we anticipate $\mathbb{R} = 2S/(AG_{th}) \simeq 30$ V/W, given $G_{th} = 7 \times 10^4$ W/K·m^2,[9] a Seebeck coefficient of $S = 50$ μV/K, and dimensions $L = 4$ μm and $W = 35$ μm. Because $S \to 0$ at $T = 0$, the PTE effect diminishes at low temperatures, making graphene an attractive material for room-temperature operation of THz detectors, potentially rivaling or exceeding existing technologies.[29]

In this study, we present a sensitive photothermal-electric (PTE)-based antenna integrated graphene photodetector (Figure 1) optimized for sub-millimeter wavelength, achieving a voltage responsivity ($\mathbb{R}$) of approximately 35 V/W at zero source-drain bias. This system features a fractional bandwidth of about 150 GHz and a noise equivalent power (NEP) at room temperature of 300 pW/$\sqrt{\text{Hz}}$. The design was refined through advanced microwave simulations and equivalent circuit modeling, leading to the implementation of a capacitively coupled dipole antenna system. We investigated two antenna configurations: narrow and wide dipole antennas, the latter hereafter referred to as the 'patch' antenna. Our analysis indicated that the dimensions of the antenna strips and the coupling capacitance significantly influence detection magnitude, resonance frequency, and operational bandwidth.

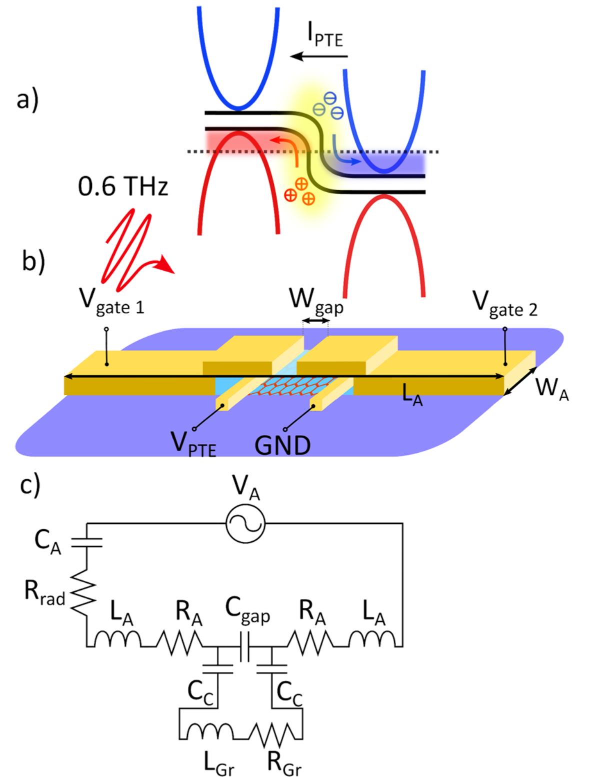

Figure 1. (a) THz dipole antenna utilizing the PTE effect in BLG as a rectification mechanism. (b) A schematic illustrating the electrical connections to the antenna, where the photovoltage (V_{PTE}) is developed between the two antenna arms with the THz field concentrated at the antenna nanogap. Voltages $V_{gate\ 1,2}$ control the carrier densities on both sides of the gap. (c) The equivalent circuit model for the antenna.

The gapped nature of BLG[30,31] plays a pivotal role in enhancing the device's sensitivity through the Seebeck effect, which behaves differently at the p–n junction compared to single-layer graphene (SLG). In BLG, the presence of a bandgap at the charge neutrality point (CNP) of approximately $\Delta \approx 250$ meV facilitates effective modulation of carrier density, enhancing THz frequency responsivity[12] through differential Seebeck effects across the p–n junction. The maximum Seebeck coefficient difference on both sides of the junction, which scales linearly with the bandgap, arises when the Fermi level crosses the conduction band in the n-region and the valence band in the p-region, boosting the photovoltage responsivity.[32] The presence of a bandgap not only enhances the Seebeck coefficient but also reduces the phonon-aided cooling due to a decreased density of available states for interband electron transitions, which diminishes completely when $\hbar\omega_{ph} = \Delta$. This reduction in phonon-aided cooling, coupled with a decrease in electronic heat conductance, leads to stronger localized electron heating (ΔT_e) hence elevating the device's responsivity ($\mathbb{R}$).

Our device utilizes quasi-free-standing bilayer graphene (BLG), produced via thermal decomposition of silicon carbide and hydrogen intercalation[33] on a silicon-carbide substrate.

https://doi.org/10.1021/acsaelm.4c00870
ACS Appl. Electron. Mater. 2024, 6, 4819−4825

This method not only ensures potentially ultralow thermal conductance but also high transparency in the THz frequency range, yielding wafer-scale graphene with enhanced carrier mobility and density. These conditions are crucial for achieving low overall resistance, vital for effective impedance matching between graphene and the receiving antenna.

We opted for BLG over single-layer graphene (SLG) due to the more effective modulation of carrier density in BLG, which enhances THz frequency responsivity.[12] The design incorporates Au split gates to electrostatically create a p−n junction within the BLG channel and to optimize THz signal coupling onto the BLG. By exploiting optical field enhancement and confinement in the antenna/split-gate nanogap, alongside impedance matching, we significantly enhance the interaction and optical absorption in the p−n junction region. This results in a confined electron heat source and elevated responsivity ($\mathbb{R}$), paving the way for high-performance THz detectors.

■ RESULTS AND DISCUSSION

Design and Simulations. To optimize the impedance matching for f = 600 GHz, we build a lumped element model[25] to calculate the input impedance of the THz antenna and estimate the maximum absorbed power in the BLG based on finite element method (FEM) simulations. The model presented in Figure 1c resembles the shape of the real dipole antenna. Showing all the components modeled and described here: the model accounts for the ohmic losses in the antenna's arm and the radiation losses (R_{ohm}, R_{rad}), the self-capacitance $C_A = \varepsilon_0 L_A / \left(\ln\frac{L_A}{W_A}\right)$ as well as the kinetic inductance of the gold ribbons $L_k = \frac{L_A}{A} Re\left(\frac{1}{\omega^2 \varepsilon_0 (1-\varepsilon_{Au})}\right)$.[34] A gap capacitance $C_{gap} = \frac{\varepsilon_0 A}{d}$ was introduced for coupling the antenna arms at the nanogap. The coupling capacitors C_C represent the capacitive coupling between the antenna's arm and the BLG and are modeled as an additional sheet inductor. The source of the two circuits is defined by the open-circuit voltage source[25] V_A, which is equal to the projection of the incident field intensity E_0 in V/m to the length of the antenna L_A ($V_A = E_0 \times L_A$). From the equivalent circuit in Figure 1c, we define an expression of the field enhancement at the nanogap $|E_{gap}|^2/|E_0|^2 = \left(\frac{l_A}{d_{gap}}\right)^2 |\frac{Z_{gap}}{Z_{gap}+Z_A}|^2$, where the enhancement is proportional to $1/d^2$. From this model, it is clear that a small antenna gap is desired. The field at the center of the nanogap V_A reaches a maximum when the reactance of the equivalent impedance at the nanogap Z_{gap} matches the dipole antenna reactance $X_A = -X_{gap}$. The gap impedance Z_{gap} comprises the graphene complex impedance Z_G. The ohmic contacts of the source and drain electrodes to the graphene sheet, R_C, and the capacitance between the antenna arms with the graphene layer, C_C, are included in Z_{gap}. The first antenna resonance is set by L_A and C_A with $f_A = 1/2\pi\sqrt{L_A C_A}$. $f_A \simeq$ 590 GHz for the dipole antenna and ≃570 GHz for the patch. The antenna operates in an open circuit at the second resonance, as X_{gap} creates a minimum of the sum of gap and antenna impedances. This is shown in Figure 2a,b where the maximum gap field intensity is correlated to the maximum input resistance. The second resonance frequency for both dipole and patch occur at 610 and 625 GHz, respectively, merging with the first antenna resonance, although it is possible to tune the second resonance frequency by changing the complex impedance of the graphene load.[25] FEM simulations were conducted in parallel to confirm the equivalent circuit model. The absorbed power density in the BLG is computed (Figure 2b) at a wide frequency range where we extract the antenna enhancement factor at the nanogap.

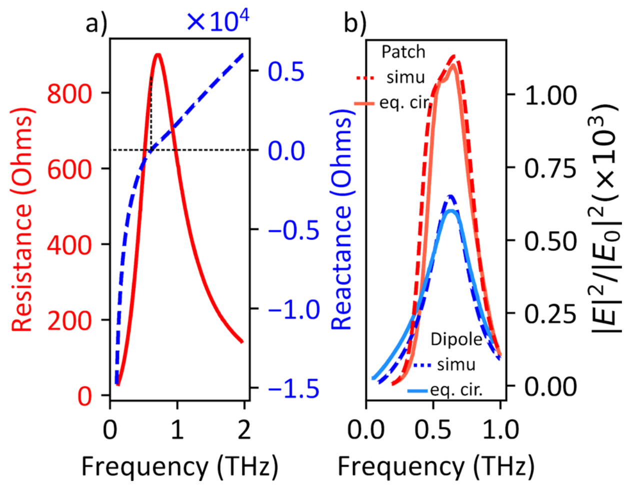

Figure 2. (a) Input resistance and reactance of the antenna are calculated from the equivalent circuit model when matched to a BLG p−n junction at 600 GHz. In the impedance matching condition, the antenna's maximum absorbed power occurs near the resonance frequency, which is also verified using FEM simulations, plotted concurrently in (b).

As PTE detectors are sensitive in the region where the graphene's chemical potential is tuned near the charge neutrality point,[10] the impedance seen by the antenna is usually much higher than for the ungated graphene channel. To simulate the impedance of the THz detector near the optimal operational point, we use a resistance sheet model[35] with an effective layer thickness d_{eff} = 2 nm and impedance at 600 GHz $Z_{sheet}(E_F = 200\text{ meV}) \sim (1k + j500)\ \Omega$/sq, ensuring that the antennas are designed to operate in a regime where the PTE detector is the most sensitive. Both 3D full wave simulation and equivalent circuit model converge to a similar antenna enhancement profile for the dipole and patch antenna. From the FEM simulations, we can extract the antennas area's effective area A_e defined as $A_e = P_{gr}/p_{in}$ (in m^2), where P_{gr} and p_{in} are the power absorbed in the graphene load and the incident THz power density (in W/m^2), respectively. Using both equivalent circuit models and FEM simulations, the optimized geometrical parameters for the dipole and patch antennas were extracted and summarized in Table 1.

Table 1. Antenna Design Physical Parameters

	Antenna Dimensions μm × μm	Channel Dimension μm × μm	Resonance Freq. GHz	BW GHz	A_e/λ^2
dipole	260 × 5	5 × 5	610	320	0.23
Patch	180 × 36	4.5 × 36	625	450	0.31

d.c. Characterizations. To establish the optimal operating conditions for our photodetector, we conducted d.c. electrical characterizations. This involved sweeping the split-gate voltages ($V_{gate\ 1}$, $V_{gate\ 2}$) while recording the device current I_{DS} and varying the source-drain bias V_{DS} from −5 to 5 V. The resistance map of a dipole (patch) antenna p−n junction

https://doi.org/10.1021/acsaelm.4c00870
ACS Appl. Electron. Mater. 2024, 6, 4819−4825

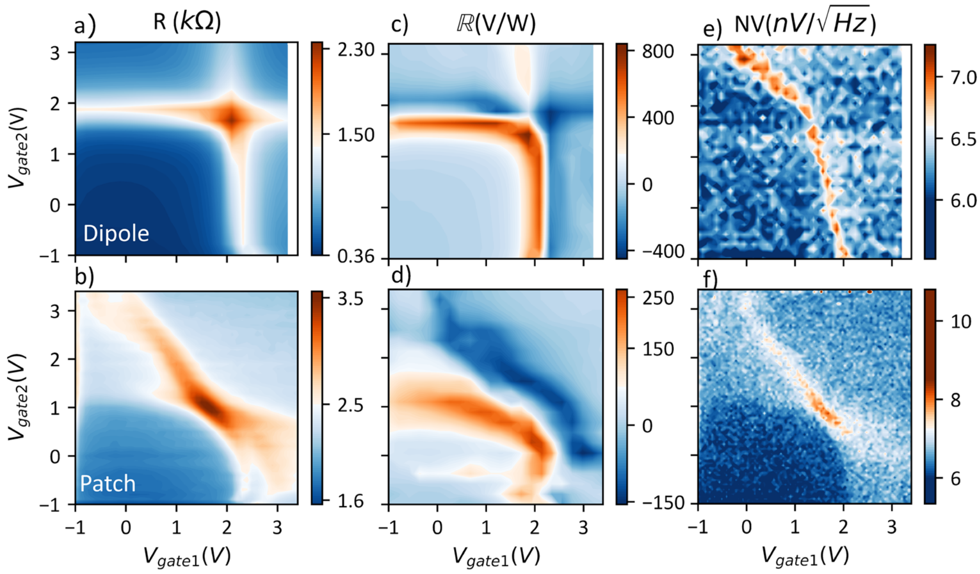

Figure 3. Transport characterizations of dipole antenna (a, c, e) and patch (b, d, f) PTE detectors at room temperature. (a, b) Resistance maps as a function of the voltage applied to two top gates, revealing four distinct regions corresponding to different doping configurations: p-n, p-p, n-p, and n-n. (c, d) Direct current (d.c.) transport responsivity, measured in volts per watt (V/W), against gate voltage without THz excitation. (e, f) A noise voltage map as a function of the gate voltage, with no terahertz excitation present.

Table 2. Comparison of Antenna-Coupled Graphene Photodetector and to Other Room-Temperature THz Sensors with Various Detection Mechanisms

Detection Mechanism	Resonance Freq (GHz)	$\mathbb{R}_{THz,max}$ (V/W)	A_e Simulation[a] μm^2	Fractional BW[a] (GHz)	NEP pW/$\sqrt{Hz}$	ref
PTE	634	15	$0.23\lambda^2$	15.8%	400	this work
PTE	600	35	$0.31\lambda^2$	28.2%	300	this work
PTE	325	30	$0.1\lambda^2$	4.6%	51	23
PTE	2800	≈6	n.c.	12.5%	∼1000	10
PTE	1800	30	$0.31\lambda^2$	n.c.	51	9
PTE	600	15	n.c.	n.c.	515	21
CMOS	650	70k	n.c.	n.c.	300	38
InGaAs Diodes	650	13	n.c.	n.c.	200	39
MEMS bolometer	250−3000		n.c.	n.c.	500	36

[a]n.c. stands for "not communicated".

detector (Figure 3a and b, respectively) displays four regions, each corresponding to different doping levels on either side of the junction. The map is symmetric, with resistance peaking at approximately $R \approx 3.5$ kΩ for the patch antenna and $R \approx 2.2$ kΩ for the dipole at the charge neutrality point (CNP), which ranges between 1.8 and 2.2 V. This reflects p-doping of the unbiased bilayer graphene (BLG) with a carrier concentration of $n \approx 1.7 \times 10^{13}$ cm^{-2} and a Fermi energy of $E_F \approx 240$ meV relative to the CNP.

The total resistance R consists of channel resistance (R_{ch}) and contact resistance (R_C). R_{ch} includes a fixed contribution from ungated BLG regions and a gate-dependent contribution from channel segments beneath the split gates. The observed gate-dependent variability in R in Figure 3a,b indicates that R_{ch} is the predominant factor, aligning with our low contact resistivity (<40 Ω·μm) for epitaxial BLG, based on channel geometry and sheet resistance measurements from independent reference samples.

To evaluate the performance of the graphene thermoelectric detector, we conducted d.c. measurements to determine the Joule heating responsivity (Figure 3c,d). A d.c. bias voltage was applied to heat the sample, and the thermoelectric current was measured by comparing electric currents under forward and reverse biases. The peak responsivity in $\mathbb{R}_{d.c.}$ occurs at low carrier densities, where Joule heating is maximal and the Seebeck coefficient is high. The measured noise voltage (NV) with no terahertz excitation for both detector types is shown in Figure 3e,f. NV arises from intrinsic device noise and amplifier noise, which are uncorrelated and combined in quadrature. Within the response bandwidth, intrinsic device noise is primarily due to thermal fluctuations and Johnson-Nyquist noise. The thermal fluctuation noise is given by $NV_{th} = \sqrt{4k_B T^2 G_{th}}$, where T is the average bridge temperature, estimated at 22pV/$\sqrt{Hz}$ for a G_{th} of 10^4 W K^{-1} m^{-2}. The Johnson-Nyquist noise contribution is $NV_{JN} = \sqrt{4k_B TR}$, calculated at 7.5nV/$\sqrt{Hz}$ at the CNP ($R = 3.6$ kΩ) for the patch antenna and 6.0nV/$\sqrt{Hz}$ ($R = 2.2$ kΩ) for the dipole antenna. Experimental noise closely matches theoretical predictions, suggesting that detector performance is Johnson-Nyquist noise-limited. From $\mathbb{R}_{d.c.}$ and measured NV, we derive an electrical NEP of 30pW/$\sqrt{Hz}$ for the patch antenna and

https://doi.org/10.1021/acsaelm.4c00870
ACS Appl. Electron. Mater. 2024, 6, 4819−4825

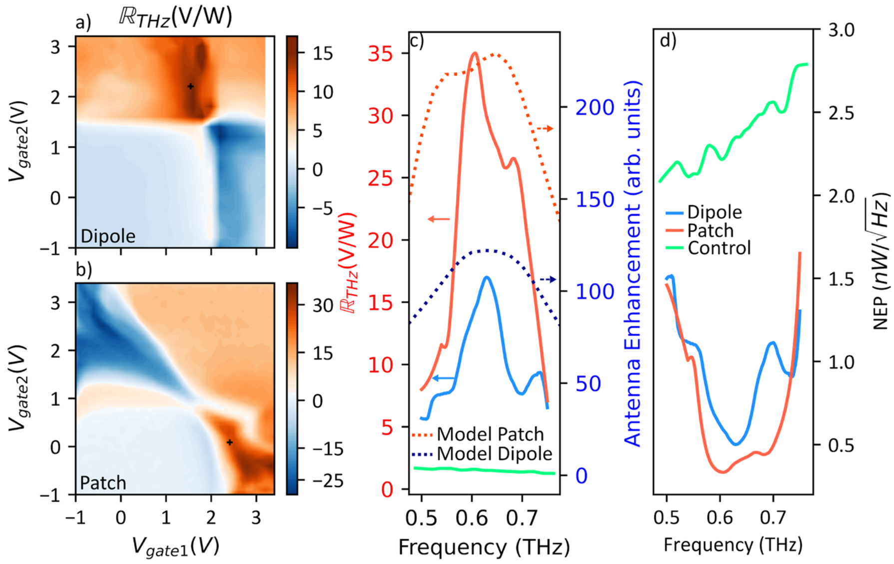

Figure 4. Responsivity maps and NEP spectra for patch and dipole antennas demonstrating PTE. (a, b) THz responsivity maps for the patch and dipole antennas, respectively, each featuring a 6-fold symmetry characteristic of the photothermal electric effect. (c) Display of the antenna-enhanced responsivity spectra. For both NEP and $\mathbb{R}_{THz}$ spectra, the used set of gate voltages is indicated in the responsivity maps in (a, b) with circles. (d) Illustrates the antenna-optimized NEP in W/Hz$^{1/2}$ for both dipole and patch antenna detectors, measured at optimal gate voltage configurations. Concurrent plots of the calculated antenna enhancement from the circuit model are provided for both types of antennas, alongside the NEP and responsivity of an unmatched antenna PTE detector (control).

7.5pW/$\sqrt{\text{Hz}}$ for the dipole antenna, comparable to the sensitivities of conventional bolometers.[36]

Optical and Spectral Characterisations. To record the terahertz (THz) responsivity of our photodetector, we aligned a continuous-wave (CW), transverse-electric (TE) polarized THz source with an aspherical lens. The photovoltage (V_{PTE}) was measured between the source and drain electrodes across the unbiased channel (V_{DS} = 0 V). Measurements were taken by varying the split-gate voltages ($V_{gate\ 1}$, $V_{gate\ 2}$) and employing a lock-in amplifier with internal modulation (square wave, ON-OFF) of the THz source at 1 kHz. The largest photoresponse occurred in the central p-n and n-p junction regimes close to the Dirac point, where the antenna's nanogap optimally channels the THz radiation.

To compute the THz responsivity ($\mathbb{R}_{THz}$), we estimated the optical power received by the bilayer graphene (BLG) based on the power intensity at the lens focus spot, defined as Intensity = P_{in}/S_A, where P_{in} is the total measured incident power and S_A is the lens focus spot area. The absorbed power by the BLG, P_{abs}, is then calculated as Intensity × A_e, with A_e being the effective aperture area determined through finite element method (FEM) simulations (Table 2). We observed maximum responsivities of about 15 V/W for the narrow dipole antenna and 35 V/W for the patch antenna (Figure 4a,b).

The shape and magnitude of both d.c. transport and optical responsivity indicate that signals originate from distinct p−n junctions within the device. Remarkably, the magnitude of $\mathbb{R}_{d.c.}$ exceeds $\mathbb{R}_{THz}$ by more than an order of magnitude, a trend also noted for the narrow dipole antenna. While we have observed significant improvements, there remains considerable potential for optimizing the quasi-optical coupling between the antenna and the lens. The response spectra of both the dipole and patch antennas are displayed in Figure 4c, with gate voltages optimized to maximize photovoltage responses at the p−n junctions (black cross in the photovoltage maps). The presence of ripples ($f_{ripples}$= 5 GHz), potentially due to the uncoated high-resistivity silicon (HR-Si) lens affecting power coupling efficiency, is noted in the measurements (Supporting Information).

Filtered spectra reveal a clear enhancement of responsivity at the antenna's resonance frequency, aligning well with the targeted frequency of 600 GHz. The spectrum's dependence of the optimization of gate voltages near the CNP, where $\mathbb{R}_{THz}$ peaks, underscores the critical role of antenna design. The responsivity spectral bandwidth correlates with the l/d ratio,[37] where l and d are the length and width of the antenna, respectively. For the dipole antenna (l/d = 26), the fractional bandwidth $\Delta f/f_0$, where Δf is the −3 dB bandwidth of the antenna resonance and f_0 is the resonance frequency, is about 15.8%, and for the patch antenna (l/d = 2.6), it increases to 28.2%

Using the extracted responsivity, we evaluated the sensitivity of the detector against the frequency of the impinging THz field (Figure 4d). By dividing the thermal noise voltage variance per 1 Hz of bandwidth by the responsivity, the noise equivalent power (NEP) was calculated as approximately 300 pW/$\sqrt{\text{Hz}}$ for the patch and 400 pW/$\sqrt{\text{Hz}}$ for the dipole antenna at their resonant frequencies at 300 K (see Figure S3 in Supporting Information). Both NEP and responsivity spectrum measurements verify that the spectral ranges where the THz detectors operate are significantly enhanced by the matched antennas compared with a control detector, which has an antenna matched at 2500 GHz, well outside the studied frequency range.

In this study, we demonstrated the capabilities of quasi-free-standing bilayer graphene (BLG) on silicon carbide (SiC) in developing antenna-enhanced graphene photodetectors. Our detectors achieved an external responsivity of approximately 35 V/W, a noise equivalent power (NEP) of about 300 pW/Hz$^{1/2}$ at 300 K, and a −3 dB spectral width of approximately 150 GHz. These results were made possible by the integration of a

https://doi.org/10.1021/acsaelm.4c00870
ACS Appl. Electron. Mater. 2024, 6, 4819−4825

terahertz (THz) antenna, which was impedance-matched to a BLG p−n junction, optimizing the light-BLG interaction and creating a confined electron heat-source that predominately generates a photothermal-electric (PTE) signal.

Our modeling of the detector architecture allowed us to maximize the absorption and $\mathbb{R}_{THz}$ at a specified frequency, while also providing the flexibility to adjust the detector's operational bandwidth. The notable improvement in NEP can be attributed to the enhanced responsivity, a direct consequence of our precise antenna design. Moreover, the high $\mathbb{R}_{d.c.}$ observed suggests that quasi-free-standing BLG on SiC is a promising material for the future development of scalable THz sensors capable of operating at room temperature. These findings not only underscore the potential of graphene-based devices in THz applications but also open avenues for further innovations in optoelectronic sensing technologies.

■ ASSOCIATED CONTENT

Supporting Information

The Supporting Information is available free of charge at https://pubs.acs.org/doi/10.1021/acsaelm.4c00870.

> Experimental methods, electrical and optical characterization of 600 GHz and 2.5 THz dipole devices, optical ray tracing simulation of the HR-Si lens, FEM simulation of the antennas, circuit model derivations, and cryogenic characterizations of the sensors at 4K (PDF)

■ AUTHOR INFORMATION

Corresponding Authors

François Joint − *Center for Nanophysics and Advanced Materials, University of Maryland, College Park, Maryland 20740, United States;* Present Address: Chalmers University of Technology, Sweden; orcid.org/0000-0002-1316-8641; Email: joint@chalmers.se

Howard D. Drew − *Center for Nanophysics and Advanced Materials, University of Maryland, College Park, Maryland 20740, United States*; Email: hdrew@umd.edu

Authors

Kunyi Zhang − *Institute for Research in Electronics and Applied Physics, University of Maryland, College Park, Maryland 20742, United States;* orcid.org/0000-0002-4233-8152

Jayaprakash Poojali − *Center for Nanophysics and Advanced Materials, University of Maryland, College Park, Maryland 20740, United States*

Daniel Lewis − *Department of Electrical and Computer Engineering, University of Maryland, College Park, Maryland 20740, United States; Institute for Research in Electronics and Applied Physics, University of Maryland, College Park, Maryland 20742, United States*

Michael Pedowitz − *Department of Electrical and Computer Engineering, University of Maryland, College Park, Maryland 20740, United States; Institute for Research in Electronics and Applied Physics, University of Maryland, College Park, Maryland 20742, United States*

Brendan Jordan − *Department of Electrical and Computer Engineering, University of Maryland, College Park, Maryland 20740, United States; Institute for Research in Electronics and Applied Physics, University of Maryland, College Park, Maryland 20742, United States*

Gyan Prakash − *Institute for Research in Electronics and Applied Physics, University of Maryland, College Park, Maryland 20742, United States*

Ashraf Ali − *Department of Physics, University of Maryland, College Park, Maryland 20742, United States*

Kevin Daniels − *Department of Electrical and Computer Engineering, University of Maryland, College Park, Maryland 20740, United States; Institute for Research in Electronics and Applied Physics, University of Maryland, College Park, Maryland 20742, United States*

Rachael L. Myers-Ward − *U.S. Naval Research Laboratory, Washington, D.C. 20375, United States*

Thomas E. Murphy − *Institute for Research in Electronics and Applied Physics, University of Maryland, College Park, Maryland 20742, United States;* orcid.org/0000-0002-8286-3832

Complete contact information is available at: https://pubs.acs.org/10.1021/acsaelm.4c00870

Notes

The authors declare no competing financial interest.

■ ACKNOWLEDGMENTS

The authors gratefully acknowledge the support and facilities provided by the staff of the University of Maryland Fabrication Laboratory. F.J. extend his deepest gratitude to Greg Jenkins for his invaluable contributions and expert guidance that significantly enhanced this work. This work was supported by the National Aeronautics and Space Administration under Grant No. 80NSSC18K0933 through the Mission Directorate. Work at the U.S. Naval Research Laboratory is supported by the Office of Naval Research.

■ REFERENCES

(1) Wiedner, M. C.; Mehdi, I.; Baryshev, A.; Belitsky, V.; Desmaris, V.; DiGiorgio, A. M.; Gallego, J.-D.; Gerin, M.; Goldsmith, P.; Helmich, F.; Jellema, W.; Laurens, A.; Risacher, C.; Cooray, A.; Meixner, M. A Proposed Heterodyne Receiver for the Origins Space Telescope. *IEEE Transactions on Terahertz Science and Technology* **2018**, *8*, 558−571.

(2) Joint, F.; Gay, G.; Vigneron, P.-B.; Vacelet, T.; Pirotta, S.; Lefevre, R.; Jin, Y.; Li, L. H.; Davies, A. G.; Linfield, E. H.; Delorme, Y.; Colombelli, R. Compact and sensitive heterodyne receiver at 2.7 THz exploiting a quasi-optical HEB-QCL coupling scheme. *Appl. Phys. Lett.* **2019**, *115*, 231104.

(3) Lopez-Fernandez, I.; Gallego-Puyol, J. D.; Diez, C.; Malo-Gomez, I.; Amils, R. I.; Fluckiger, R.; Marti, D.; Hesper, R. A 16 GHz Bandwidth Cryogenic IF Amplifier with 4-K Noise Temperature for Sub-mm Radio-Astronomy Receivers. *IEEE Transactions on Terahertz Science and Technology* **2024**, *14*, 336.

(4) Belitsky, V.; Bylund, M.; Desmaris, V.; Ermakov, A.; Ferm, S.-E.; Fredrixon, M.; Krause, S.; Lapkin, I.; Meledin, D.; Pavolotsky, A.; et al. ALMA Band 5 receiver cartridge-Design, performance, and commissioning. *Astronomy Astrophysics* **2018**, *611*, A98.

(5) Yan, J.; Kim, M.-H.; Elle, J. A.; Sushkov, A. B.; Jenkins, G. S.; Milchberg, H. M.; Fuhrer, M. S.; Drew, H. D. Dual-gated bilayer graphene hot-electron bolometer. *Nat. Nanotechnol.* **2012**, *7*, 472−478.

(6) Miao, W.; Gao, H.; Wang, Z.; Zhang, W.; Ren, Y.; Zhou, K. M.; Shi, S. C.; Yu, C.; He, Z. Z.; Liu, Q. B.; Feng, Z. H. A Graphene-Based Terahertz Hot Electron Bolometer with Johnson Noise Readout. *Journal of Low Temperature Physics* **2018**, *193*, 387−392.

(7) Lara-Avila, S.; Danilov, A.; Golubev, D.; He, H.; Kim, K. H.; Yakimova, R.; Lombardi, F.; Bauch, T.; Cherednichenko, S.; Kubatkin, S. Towards quantum-limited coherent detection of

terahertz waves in charge-neutral graphene. *Nature Astronomy* **2019**, *3*, 983−988.

(8) Cai, X.; Sushkov, A. B.; Suess, R. J.; Jadidi, M. M.; Jenkins, G. S.; Nyakiti, L. O.; Myers-Ward, R. L.; Li, S.; Yan, J.; Gaskill, D. K.; Murphy, T. E.; Drew, H. D.; Fuhrer, M. S. Sensitive room-temperature terahertz detection via the photothermoelectric effect in graphene. *Nat. Nanotechnol.* **2014**, *9*, 814−819.

(9) Castilla, S.; Terrés, B.; Autore, M.; Viti, L.; Li, J.; Nikitin, A. Y.; Vangelidis, I.; Watanabe, K.; Taniguchi, T.; Lidorikis, E.; Vitiello, M. S.; Hillenbrand, R.; Tielrooij, K.-J.; Koppens, F. H. Fast and Sensitive Terahertz Detection Using an Antenna-Integrated Graphene pn Junction. *Nano Lett.* **2019**, *19*, 2765−2773.

(10) Asgari, M.; Riccardi, E.; Balci, O.; De Fazio, D.; Shinde, S. M.; Zhang, J.; Mignuzzi, S.; Koppens, F. H. L.; Ferrari, A. C.; Viti, L.; Vitiello, M. S. Chip-Scalable, Room-Temperature, Zero-Bias, Graphene-Based Terahertz Detectors with Nanosecond Response Time. *ACS Nano* **2021**, *15*, 17966−17976.

(11) Skoblin, G.; Sun, J.; Yurgens, A. Graphene bolometer with thermoelectric readout and capacitive coupling to an antenna. *Appl. Phys. Lett.* **2018**, *112*, No. 063501.

(12) Spirito, D.; Coquillat, D.; De Bonis, S. L.; Lombardo, A.; Bruna, M.; Ferrari, A. C.; Pellegrini, V.; Tredicucci, A.; Knap, W.; Vitiello, M. S. High performance bilayer-graphene terahertz detectors. *Appl. Phys. Lett.* **2014**, *104*, No. 061111.

(13) Bandurin, D. A.; Gayduchenko, I.; Cao, Y.; Moskotin, M.; Principi, A.; Grigorieva, I. V.; Goltsman, G.; Fedorov, G.; Svintsov, D. Dual origin of room temperature sub-terahertz photoresponse in graphene field effect transistors. *Appl. Phys. Lett.* **2018**, *112*, 141101.

(14) Bandurin, D. A.; et al. Resonant terahertz detection using graphene plasmons. *Nat. Commun.* **2018**, *9*, 5392.

(15) Auton, G.; But, D. B.; Zhang, J.; Hill, E.; Coquillat, D.; Consejo, C.; Nouvel, P.; Knap, W.; Varani, L.; Teppe, F.; Torres, J.; Song, A. Terahertz Detection and Imaging Using Graphene Ballistic Rectifiers. *Nano Lett.* **2017**, *17*, 7015−7020.

(16) Hemmetter, A.; Yang, X.; Wang, Z.; Otto, M.; Uzlu, B.; Andree, M.; Pfeiffer, U.; Vorobiev, A.; Stake, J.; Lemme, M. C.; Neumaier, D. Terahertz Rectennas on Flexible Substrates Based on One-Dimensional Metal−Insulator−Graphene Diodes. *ACS Applied Electronic Materials* **2021**, 3, 3747−3753.

(17) Hsu, A. L.; Herring, P. K.; Gabor, N. M.; Ha, S.; Shin, Y. C.; Song, Y.; Chin, M.; Dubey, M.; Chandrakasan, A. P.; Kong, J.; Jarillo-Herrero, P.; Palacios, T. Graphene-Based Thermopile for Thermal Imaging Applications. *Nano Lett.* **2015**, *15*, 7211−7216.

(18) Hwang, E. H.; Rossi, E.; Das Sarma, S. Theory of thermopower in two-dimensional graphene. *Phys. Rev. B* **2009**, *80*, 235415.

(19) Nam, S.-G.; Ki, D.-K.; Lee, H.-J. Thermoelectric transport of massive Dirac fermions in bilayer graphene. *Phys. Rev. B* **2010**, *82*, 245416.

(20) Zuev, Y. M.; Chang, W.; Kim, P. Thermoelectric and Magnetothermoelectric Transport Measurements of Graphene. *Phys. Rev. Lett.* **2009**, *102*, No. 096807.

(21) Zak, A.; Andersson, M. A.; Bauer, M.; Matukas, J.; Lisauskas, A.; Roskos, H. G.; Stake, J. Antenna-Integrated 0.6 THz FET Direct Detectors Based on CVD Graphene. *Nano Lett.* **2014**, *14*, 5834−5838.

(22) Lucas, A.; Fong, K. C. Hydrodynamics of electrons in graphene. *J. Phys.: Condens. Matter* **2018**, *30*, No. 053001.

(23) Qin, H.; Sun, J.; Liang, S.; Li, X.; Yang, X.; He, Z.; Yu, C.; Feng, Z. Room-temperature, low-impedance and high-sensitivity terahertz direct detector based on bilayer graphene field-effect transistor. *Carbon* **2017**, *116*, 760−765.

(24) Eggleston, M. S.; Messer, K.; Zhang, L.; Yablonovitch, E.; Wu, M. C. Optical antenna enhanced spontaneous emission. *Proc. Natl. Acad. Sci. U. S. A.* **2015**, *112*, 1704−1709.

(25) Bettenhausen, M.; Grüßing, S.; Hardt, E.; Flesch, J.; Römer, F.; Chavarin, C. A.; Klesse, W. M.; You, C.; Piehler, J.; Capellini, G.; Witzigmann, B. Impedance Matching of THz Plasmonic Antennas. *Journal of Infrared, Millimeter, and Terahertz Waves* **2019**, *40*, 929−942.

(26) Mišeikis, V.; et al. Ultrafast, Zero-Bias, Graphene Photodetectors with Polymeric Gate Dielectric on Passive Photonic Waveguides. *ACS Nano* **2020**, *14*, 11190−11204.

(27) El Fatimy, A.; Myers-Ward, R. L.; Boyd, A. K.; Daniels, K. M.; Gaskill, D. K.; Barbara, P. Epitaxial graphene quantum dots for high-performance terahertz bolometers. *Nat. Nanotechnol.* **2016**, *11*, 335−338.

(28) Mak, K. F.; Lui, C. H.; Heinz, T. F. Measurement of the thermal conductance of the graphene/SiO_2 interface. *Appl. Phys. Lett.* **2010**, *97*, No. 221904.

(29) Liu, J.; Li, X.; Jiang, R.; Yang, K.; Zhao, J.; Khan, S. A.; He, J.; Liu, P.; Zhu, J.; Zeng, B. Recent Progress in the Development of Graphene Detector for Terahertz Detection. *Sensors* **2021**, *21*, 4987.

(30) Kim, K. S.; Walter, A. L.; Moreschini, L.; Seyller, T.; Horn, K.; Rotenberg, E.; Bostwick, A. Coexisting massive and massless Dirac fermions in symmetry-broken bilayer graphene. *Nature materials* **2013**, *12*, 887−892.

(31) Ohta, T.; Bostwick, A.; Seyller, T.; Horn, K.; Rotenberg, E. Controlling the electronic structure of bilayer graphene. *Science* **2006**, *313*, 951−954.

(32) Titova, E.; Mylnikov, D.; Kashchenko, M.; Safonov, I.; Zhukov, S.; Dzhikirba, K.; Novoselov, K. S.; Bandurin, D. A.; Alymov, G.; Svintsov, D. Ultralow-noise Terahertz Detection by p−n Junctions in Gapped Bilayer Graphene. *ACS Nano* **2023**, *17*, 8223−8232.

(33) Emery, J. D.; Wheeler, V. D.; Johns, J. E.; McBriarty, M. E.; Detlefs, B.; Hersam, M. C.; Kurt Gaskill, D.; Bedzyk, M. J. Structural consequences of hydrogen intercalation of epitaxial graphene on SiC(0001). *Appl. Phys. Lett.* **2014**, *105*, 161602.

(34) Kraus, J. D. *Antennas;* McGraw-Hill Inc., 1988.

(35) Yang, Z.; Yuan, X.-W.; Huang, X.-W.; Yang, M.-L.; Sheng, X.-Q. Resistive Sheet Boundary Condition-Based Nonconformal Domain Decomposition FE-BI-MLFMA for Electromagnetic Scattering From Inhomogeneous Objects With Honeycomb Structures. *IEEE Transactions on Antennas and Propagation* **2022**, *70*, 9483−9496.

(36) Zhang, Y.; Hosono, S.; Nagai, N.; Song, S.-H.; Hirakawa, K. Fast and sensitive bolometric terahertz detection at room temperature through thermomechanical transduction. *J. Appl. Phys.* **2019**, *125*, 151602.

(37) Balanis, C. A. *Antenna theory: analysis and design,* 3rd ed.; John Wiley: Hoboken, NJ, 2005.

(38) Lisauskas, A.; Pfeiffer, U.; Öjefors, E.; Bolìvar, P. H.; Glaab, D.; Roskos, H. G. Rational design of high-responsivity detectors of terahertz radiation based on distributed self-mixing in silicon field-effect transistors. *J. Appl. Phys.* **2009**, *105*, 114511.

(39) Palenskis, V.; Minkevičius, L.; Matukas, J.; Jokubauskis, D.; Pralgauskaitė, S.; Seliuta, D.; Čechavičius, B.; Butkutė, R.; Valušis, G. InGaAs diodes for terahertz sensing—Effect of molecular beam epitaxy growth conditions. *Sensors* **2018**, *18*, 3760.

https://doi.org/10.1021/acsaelm.4c00870
ACS Appl. Electron. Mater. 2024, 6, 4819−4825